Editors' Suggestion

Dynamical phase transitions across slow and fast regimes in a two-tone driven Duffing resonator

Soumya S. Kumar [1,*] Javier del Pino [1,2] Letizia Catalini [3,4,5] Alexander Eichler [3,4] and Oded Zilberberg [1,†]

[1]*Department of Physics, University of Konstanz, 78464 Konstanz, Germany*

[2]*Departamento de Física Teórica de la Materia Condensada and Condensed Matter Physics Center (IFIMAC), Universidad Autónoma de Madrid, E-28049 Madrid, Spain*

[3]*Laboratory for Solid State Physics, ETH Zürich, 8093 Zürich, Switzerland*

[4]*Quantum Center, ETH Zürich, 8093 Zürich, Switzerland*

[5]*Center for Nanophotonics, AMOLF, 1098XG Amsterdam, The Netherlands*

(Received 17 February 2026; accepted 29 April 2026; published 15 June 2026)

The response of nonlinear resonators to multifrequency driving reveals rich dynamics beyond conventional single-tone theory. We study a Duffing resonator under bichromatic excitation and identify a competition between the two drives, governed by their detuning and relative amplitudes. In the slow-beating regime, where the tones are closely spaced, the secondary tone acts as a modulation that induces dynamical phase transitions between coexisting stationary states. We introduce the cycle-averaged amplitude as an order parameter and map the resulting phase diagram as a function of the drive detuning and amplitude ratio, capturing the pronounced asymmetry observed for blue versus red detuning between the drives in experiment. We link the onset of these transitions to the resonance properties around the nonlinear stationary mode of the system. We apply a two-tone ansatz to this system, for the first time, to provide a comprehensive map of stationary states. Our results provide a framework for controlling driven nonlinear systems, enabling state manipulation, and sensing in nanomechanical, optical, and superconducting circuit platforms.

DOI: 10.1103/d3b6-lnw6

I. INTRODUCTION

Nonlinear driven-dissipative systems, where coherent external drives compete with inherent dissipation and nonlinearity [1,2], are ideal for exploring diverse nonequilibrium phenomena relevant for climate physics [3], population dynamics [4,5], nanotechnology [6], optics [7,8], and quantum technologies [9]. Nonlinear dynamical behavior such as bursting oscillations or relaxation-like cycles [10], characterized by alternating high-amplitude and low-amplitude activity, is observed in aerosol-cloud-precipitation systems [11], circadian rhythms of various organisms [12], and even optical fiber lasers subjected to weak optical injection [13].

Multi-tone driving of nonlinear systems is ubiquitous: In microelectromechanical and nanoelectromechanical resonators, it enables the study of synchronization and chaos, and is widely used in precision metrology and sensing [14–20]; in ultracold atoms, it enables topological bands and Floquet-engineered states with controlled heating [21–23]; it supports quantum memcapacitors in superconducting circuits [24]; it generates magnonic frequency combs in magnomechanical systems [25]; and it is a powerful tool to study dynamical phase transitions [26]. Such systems of slow, periodically forced resonators have been extensively studied in the context of mixed-mode oscillations [27,28]. Even a simple two-tone driven Duffing resonator gives rise to complex dynamical behavior that is not captured by existing methods [19,29–32]. This complex behavior, arising due to the interplay of dissipation, two drive tones, and nonlinearity, has led to sensing proposals [20,29], realization of chaos [30], and even controlled transitions in multi-modal resonators [32]. Despite this ubiquity, a systematic analysis that maps behaviors to parameter regimes is missing.

Our understanding of nonlinear driven-dissipative systems is largely built on their response to single-tone driving. Traditional approaches to analyzing these systems rely on approximations that simplify the dynamics, such as the rotating-wave approximation or timescale separation, which neglect fast oscillating terms [33]. While these approximations can be effective for single-frequency systems, they may not accurately capture the dynamics due to multiple tones. As such, established perturbative methods like Krylov-Bogoliubov [34,35], Poincaré-Lindstedt [36], and others, while valuable for weakly nonlinear single-tone systems or systems involving commensurate frequencies, are insufficient to capture dynamics arising due to incommensurate, low-detuned multi-tone drives where subdominant driving responses are usually treated as linear perturbations.

Recently, the complex trajectories of a two-tone driven Duffing resonator were examined through the lens of the changing phase-space flow [31]. A slow regime was identified where the system follows the flow to encircle coexisting attractors, in contrast to a fast regime where such global orbits

*Contact author: soumya.kumar@uni-konstanz.de

†Contact author: oded.zilberberg@uni-konstanz.de

Published by the American Physical Society under the terms of the Creative Commons Attribution 4.0 International license. Further distribution of this work must maintain attribution to the author(s) and the published article's title, journal citation, and DOI.

are suppressed. While this perspective provides geometric intuition, it relies on a phenomenological reconstruction of the dynamics. A predictive framework that maps the boundaries of these dynamical phase transitions based on the resonator's response function is currently lacking.

In this work, we develop an effective nonlinear response theory around driven stationary states to predict the thresholds for dynamical phase transitions. To this end, we first revisit the theory of linear and nonlinear response to establish the modified equations of motion. We then introduce an order parameter to map the dynamical phase diagram as a function of the detuning and relative strength of the secondary tone. Crucially, we extract an analytical threshold for the onset of these transitions, providing a vital tool for experimentalists to identify stable operating regimes. Furthermore, we apply a two-tone ansatz for the first time to this system, elucidating the complex dynamical responses beyond the reach of standard approximations. Our results leverage a linear-theory-based approach to gain insight into the dynamics of a two-tone driven Duffing resonator. These results have implications across fields of physics in sensing and metrology, nonlinear optomechanics, optimized control of qubits, circuit quantum electrodynamics, and Floquet engineering in ultracold atoms [21,29,37–39]. They are also important beyond physics in the study of tipping points in the context of early warning signs in climate dynamics, ecological systems, and socioeconomic models [4,40–42].

The remainder of this paper is structured as follows: In Sec. II, we introduce our model system: a Duffing resonator subject to a bichromatic drive. To build intuition, we first revisit the linear regime of the system in Sec. III, establishing a rotating frame formalism that reveals how the two tones interact in the absence of nonlinearity. In Sec. IV, we review the canonical single-tone driven Duffing resonator, detailing the harmonic balance method (HBM) used for its analysis. In Sec. V, we analyze the slow-beating regime, treating the secondary tone as a slow modulation that can induce dynamical phase transitions, and we introduce an order parameter to map out the resulting phase diagram. In Sec. VI, we refine a linear-response-based approach with nonlinear corrections to analytically approximate the observed transition boundaries. In Sec. VII, we apply an extended (two-tone) ansatz to this system for the first time to provide a comprehensive map of stationary states and connect the results with the analytical boundaries in Sec. VI. Finally, we conclude in Sec. VIII with a summary of our key findings and an outlook on future research directions.

II. SYSTEM

The dynamics of a nonlinear Duffing (Kerr) resonator, subject to a bichromatic (two-tone) drive, is described by the equation of motion

$$\ddot{x} + \Omega_0^2 x + \Gamma \dot{x} + \alpha x^3 = \sum_{i=1,2} \mathrm{Re}[F_i e^{i(\Omega_i t + \theta_i)}]. \tag{1}$$

Here, x denotes the resonator displacement, Ω_0 is the natural resonance frequency, Γ represents the damping coefficient, and α is the Duffing nonlinearity. We work in units where the resonator mass is $m = 1$. The system is driven by two tones with amplitudes F_i, frequencies Ω_i, and phases θ_i, where $i = 1, 2$.

The sign of the Duffing coefficient α dictates the nature of the nonlinearity: $\alpha < 0$ ($\alpha > 0$) corresponds to a softening (hardening) spring characteristic with increasing displacement. This sign also governs qualitative changes in the potential energy landscape of the resonator [see Fig. 1(a)]. Our analysis considers the weak nonlinearity regime, where the quartic term remains a perturbation to the harmonic potential. Furthermore, we assume a negative Duffing nonlinearity $\alpha < 0$; a similar analysis for $\alpha > 0$ will yield qualitatively similar results under proper tuning of parameters.

III. TWO-TONE LINEAR RESPONSE THEORY

We first revisit the linear response of a resonator driven by two tones. The equation of motion of a linear damped resonator [$\alpha = 0$ in Eq. (1)] is readily solved in Fourier space [43], where the resulting Fourier amplitude of the system reads

$$\tilde{x}(\omega) = \sum_{i=1,2} F_i \chi_{\Omega_0}(\omega) \delta(\Omega_i - \omega), \tag{2}$$

with $\chi_{\Omega_0}(\omega) = (\Omega_0^2 - \omega^2 - i\Gamma\omega)^{-1}$ the susceptibility of the damped harmonic resonator [44], which characterizes the resonator's inherent frequency-dependent response [see Fig. 1(b)]. In linear systems, the equation of motion precludes frequency mixing. Consequently, the total response (2) is a superposition of individual responses. The response amplitude (and thus the power) depends on the drive strength F_i, the resonator susceptibility $\chi_{\Omega_0}(\omega)$, and the detuning [see Fig. 1(b)]. The response diminishes as the drive frequency deviates from Ω_0. Hence, the combined effects of its strength and detuning determine which drive leads to a stronger response.

To further analyze the system's response to the two driving tones, we first assume that the drive F_1 (at frequency Ω_1) elicits the dominant response. Accordingly, we reformulate the problem in a frame corotating with this main drive component. To this end, the resonator's displacement $x(t)$ is expressed via the transformation

$$x(t) = X(t)\cos\Omega_1 t - Y(t)\sin\Omega_1 t, \tag{3}$$

where $X(t)$ and $Y(t)$ are the time-dependent resonator quadratures. We decompose the overall drive $F(t)$ from Eq. (1) relative to Ω_1 as

$$F(t) = \mathrm{Re}[e^{i(\Omega_1 t + \theta_1)}(1 + he^{i(\Delta_{21} t + \theta_2 - \theta_1)})]F_1, \tag{4}$$

where $\Delta_{21} = \Omega_2 - \Omega_1$ is the detuning between the drive frequencies and $h = \frac{F_2}{F_1}$ is the relative strength of the two tones.

Substituting the transformation (3) into the linear equation of motion [Eq. (1), with $\alpha = 0$], we obtain the coupled equations for the quadratures by equating the coefficients of the $\sin(\Omega_1 t)$ and $\cos(\Omega_1 t)$ contributions independently:

$$\begin{bmatrix} \ddot{X} \\ \ddot{Y} \end{bmatrix} + \begin{bmatrix} \Gamma & 2\Omega_1 \\ -2\Omega_1 & \Gamma \end{bmatrix} \begin{bmatrix} \dot{X} \\ \dot{Y} \end{bmatrix} + \begin{bmatrix} \tilde{\Delta}_{01}^2 & \Gamma\Omega_1 \\ -\Gamma\Omega_1 & \tilde{\Delta}_{01}^2 \end{bmatrix} \begin{bmatrix} X \\ Y \end{bmatrix} = \vec{F}, \tag{5}$$

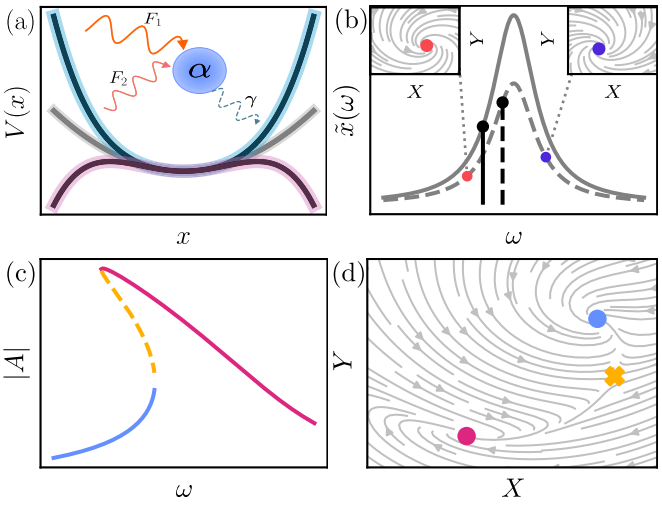


FIG. 1. The Duffing resonator's linear response to two drives and nonlinear response to a single drive. (a) Potential energy landscape $V(x)$ of a Duffing resonator [cf. Eq. (1)] with positive (blue), vanishing (gray), and negative (red) nonlinearity α. Inset: Sketch of a Duffing resonator subject to two different drives (wavy inbound arrows) and dissipation (dashed outbound arrow). (b) Stationary amplitude $\tilde{x}(\omega)$ of a linear resonator driven by two tones [cf. Eq. (2)]. The solid and dashed curves represent the scaled susceptibility $F_i\chi_{\Omega_0}(\omega)$ for different drive strengths F_i. Note that a weaker drive closer to resonance (dashed) can yield a higher response than a stronger detuned drive (solid). Insets: Rotating frame vector flow [cf. Eq. (5)]; a positively detuned drive induces clockwise motion, while a negatively detuned one induces anticlockwise motion. (c) Single-tone nonlinear response [cf. Eq. (9)] exhibiting bistability between low (blue) and high (pink) amplitude branches, separated by an unstable saddle (yellow dashed). We use $\Omega_0 = 2\pi$, $\Gamma = 6.2 \times 10^{-4}$, and $F_1 = 4.81 \times 10^{-4}$. (d) Phase space vector flow (gray lines) for a drive fixed in the bistable region ($\Delta_{10} = -9.02 \times 10^{-4}$), showing two counterrotating attractors (pink and blue dots) separated by a saddle (yellow cross).

with effective force $\vec{F} = F_1[1 + h\cos(\Delta_{21}t), -h\sin(\Delta_{21}t)]^T$ written in the Ω_1-frame, with $\tilde{\Delta}_{01} = \sqrt{\Omega_0^2 - \Omega_1^2}$. These *harmonic equations* for the quadratures can be used to visualize the vector flow in a two-dimensional (2D) rotating phase space, as is measured in experiments with a lock-in amplifier [45]. Closed-loop stationary orbits in the phase space of the laboratory frame appear as stable states, i.e., fixed-point attractors, in the rotating phase space spanned by the quadratures $X(t)$ and $Y(t)$. Additionally, a negatively detuned drive results in an anticlockwise vector flow around the attractor, whereas a positively detuned drive leads to a clockwise vector flow [see insets in Fig. 1(b)], lending a notion of *chirality* to the attractor in the rotating frame [46–49].

The dynamics of the quadratures, governed by Eq. (5), directly determine the time-dependent squared amplitude of the resonator's response in the rotating frame, $A^2_{\Omega_0}(t,h) = X^2(t,h) + Y^2(t,h)$, which quantifies the power measured with a lock-in amplifier at Ω_1. To find $A^2_{\Omega_0}(t,h)$, we first solve Eq. (5) for $\tilde{X}(\omega)$ and $\tilde{Y}(\omega)$ via Fourier transformation. A further inverse Fourier transform yields (cf. Appendix A for details)

$$A^2_{\Omega_0}(t,h) = F_1^2(1|\chi_1|^2 + h^2|\chi_2|^2) + 2F_1^2 h|\chi_1|^2|\chi_2|^2 \times [a_{\Omega_0}\cos(\Delta_{21}t) + b_{\Omega_0}\sin(\Delta_{21}t)], \quad (6)$$

where $\chi_i \equiv \chi_{\Omega_0}(\omega = \Omega_i)$ is the resonator susceptibility at the drive frequency Ω_i and

$$a_{\Omega_0} = |\chi_1|^2 + \Delta_{21}\left[\Gamma^2\Omega_1 + (\Delta_{21} + 2\Omega_1)\left(\Omega_1^2 - \Omega_0^2\right)\right], \quad (7)$$

$$b_{\Omega_0} = \Gamma\Delta_{21}\left[\Omega_1(\Delta_{21} + \Omega_1) + \Omega_0^2\right]. \quad (8)$$

Crucially, Eq. (6) reveals that although the linear resonator responds to each drive tone independently, the power associated with the Ω_1 component of motion is not simply the direct response $F_1^2|\chi_1|^2$. Instead, $A^2_{\Omega_0}(t,h)$ incorporates two additional contributions from the secondary tone (F_2, Ω_2): (1) a static term $F_2^2|\chi_2|^2$ and (2) a time-dependent cross term proportional to F_1F_2 that originates from the beating between the two drive frequencies. This cross term signifies a temporal modulation of the primary response amplitude by the secondary tone.

IV. NONLINEAR SINGLE-TONE RESPONSE

While the linear response to two tones already exhibits complex temporal dynamics [cf. Eq. (6)], the introduction of the nonlinearity fundamentally alters the system's behavior. For a Duffing resonator driven by a single drive [$F_2 = 0$ in Eq. (1)], the nonlinear cubic term induces frequency mixing, i.e., the generation of new frequency components such as harmonics of the input frequency [36]. This precludes an exact analytical solution via Fourier transformation. However, approximate analytical solutions can be obtained via perturbative methods such as the Krylov-Bogoliubov method [34,35], the Poincaré-Lindstedt method [50], secular perturbation theory [2,51], or the HBM [52]. These methods rely on separating the timescale dominating the stationary system response from the faster timescales determined by the resonance frequency or the drive acting on the system.

In this section, we use the HBM that involves (1) switching to the rotating quadratures via Eq. (3), (2) assuming the quadratures evolve on a timescale T much larger than the system oscillations ($T \gg \frac{2\pi}{\Omega_1}$) [thereby rendering $X(t) \to X(T)$, $Y(t) \to Y(T)$], such that their variation over a single drive cycle ($2\pi/\Omega_1$) is small, and finally (3) "balancing harmonics," i.e., matching terms with harmonics rotating at the same frequency Ω_1 [53]. This slow-evolution ansatz (integral to many perturbative approaches) justifies neglecting higher-order time derivatives of the quadratures (i.e., $\ddot{X}, \ddot{Y} \approx 0$). The resulting autonomous system of two coupled first-order differential equations reads

$$\begin{bmatrix}\dot{X}\\ \dot{Y}\end{bmatrix} = \begin{bmatrix}-\frac{\Gamma}{2} & \frac{3\alpha A^2 + 4\tilde{\Delta}_{01}^2}{8\Omega_1}\\ -\frac{3\alpha A^2 + 4\tilde{\Delta}_{01}^2}{8\Omega_1} & -\frac{\Gamma}{2}\end{bmatrix}\begin{bmatrix}X\\ Y\end{bmatrix} + \frac{\vec{F}_1}{2\Omega_1} \quad (9)$$

in terms of the response amplitude $A = \sqrt{X^2 + Y^2}$ at frequency Ω_1, with $\vec{F}_1 = F_1[\sin\theta_1, \cos\theta_1]^T$.

The stationary states for the single-tone driven Duffing resonator are found by setting $\dot{X} = \dot{Y} = 0$ in Eq. (9). The drive strength F_1 and frequency Ω_1 determine the system's stationary characteristics, including the response amplitude

and the location of bifurcation points. At low driving strengths, the Duffing exhibits a quasilinear response, resembling a tilted Lorentzian. Increasing F_1 causes the response to bifurcate, leading to a high-amplitude branch and a low-amplitude branch, where a branch is a continuum of stationary states as a function of a system parameter. This bifurcation underlies the characteristic "shark-fin" profile observed when plotting the response amplitude against the drive frequency [see Fig. 1(c)]. The dynamics governed by Eq. (9) can be visualized as a 2D vector flow in phase space [see Fig. 1(d)]. When the system is in the bistable region, there are two attractors in phase space with opposite chirality: 1 (−1) for the clockwise (anticlockwise) high (low)-amplitude state [49].

We find the frequency range in which bistability occurs by analyzing the number of real roots of the response amplitude equation [54], which is accomplished by combining the two stationary conditions in Eq. (9) into

$$A^2\left(\Gamma^2+\left(\frac{3\alpha A^2}{4\Omega_1}+\frac{\Omega_0^2-\Omega_1^2}{\Omega_1}\right)^2\right)=\frac{F_1^2}{\Omega_1^2}. \tag{10}$$

This equation is a cubic polynomial in A^2. The number of its real solutions, corresponding to the stable and unstable states, changes when its discriminant vanishes. This occurs at two distinct saddle-node bifurcations, where the low- and high-amplitude branches lose stability. This vanishing discriminant condition reads

$$|F_{\mathrm{lb/hb}}|^2=\frac{8}{81\alpha}\left[\left(\tilde{\Delta}_{01}^4-3\Gamma^2\Omega_1^2\right)^{\frac{3}{2}}\pm\tilde{\Delta}_{01}^2\left(\tilde{\Delta}_{01}^4+9\Gamma^2\Omega_1^2\right)\right] \tag{11}$$

and establishes the relationship between the critical drive strength $|F_{\mathrm{lb/hb}}|^2$ for the low/high-amplitude branch to bifurcate and the bifurcation frequencies Ω_1, where the instability occurs. Thus, we can explicitly define the drive strength required to induce a bifurcation at a given frequency, or conversely, the frequencies at which bifurcations occur for a fixed drive strength. Crucially, for fixed $(\Delta_{01}, \Gamma, \Omega_1, \alpha)$, these thresholds are not equal: To jump up (low amplitude → high amplitude), the drive amplitude F_1 must exceed F_{lb}, while to jump down (high → low) it must be reduced below F_{hb}. Thus, sweeping the drive amplitude traces a hysteresis loop with direction-dependent switching.

V. TWO-TONE NONLINEAR RESPONSE

We now address the nonlinear Duffing resonator subject to a two-tone drive. A fundamental challenge in the two-tone driven Duffing resonator is that transforming to a corotating frame at a single drive frequency does not yield an autonomous system of equations. This inherent nonautonomy was already evident in the linear case [cf. Eqs. (4) and (6)]; it occurs because a single rotating frame cannot simultaneously eliminate the time dependence from both drive frequencies. This complicates the determination of stationary states, as the problem cannot be directly reduced to solving a time-independent algebraic system for fixed ansatz amplitudes, in contrast to the single-tone scenario [cf. Eq. (9)].

To analyze the two-tone driven nonlinear resonator, we first adapt the methodology previously applied to the linear case under the assumption that the drive F_1 at frequency Ω_1 generates the dominant response. This involves three key steps: (1) We employ the single-tone rotating ansatz [cf. Eq. (3)]. (2) We write the decomposed drive [Eq. (4)] as $F(t)=\mathrm{Re}[e^{i(\Omega_1 t+\theta_1)}(1+he^{i(\varphi(t)+\theta_2-\theta_1)})]F_1$. Then, we assume that the time-evolving beating phase, $\varphi(t)=\Delta_{21}t$, varies slowly relative to the primary tone's period $T=2\pi/\Omega_1$, i.e., $\Delta_{21}\ll\Omega_1$. (3) We average over the timescale T, corresponding to the primary tone's period. Crucially, we still account for the slow time variation of the beating phase as $\varphi(T)$, and write the following equations of motion for the quadratures:

$$\begin{bmatrix}\dot{X}\\ \dot{Y}\end{bmatrix}=\begin{bmatrix}-\frac{\Gamma}{2} & \frac{3\alpha A^2+4\tilde{\Delta}_{01}^2}{8\Omega_1}\\ -\frac{3\alpha A^2+4\tilde{\Delta}_{01}^2}{8\Omega_1} & -\frac{\Gamma}{2}\end{bmatrix}\begin{bmatrix}X\\ Y\end{bmatrix}+\vec{F}_{\mathrm{eff}}, \tag{12}$$

where

$$\vec{F}_{\mathrm{eff}}=\frac{F_1}{2\Omega_1}\begin{bmatrix}\sin\theta_1+h\sin(\varphi(T)+\theta_2)\\ \cos\theta_1+h\cos(\varphi(T)+\theta_2)\end{bmatrix}. \tag{13}$$

Importantly, this approach differs from the single-tone HBM used in Sec. IV, where a single-harmonic ansatz would average out responses at frequencies other than Ω_1 and thus fail to capture the dynamics induced by the secondary tone through $\varphi(T)=\Delta_{21}T$.

The time-dependent phase $\varphi(T)$ in $\vec{F}_{\mathrm{eff}}$ [cf. Eq. (13)] implies that the secondary tone acts as an amplitude modulation of the primary tone in the Ω_1-rotating frame [see Fig. 2(a)]. This modulation's effect is most clearly understood in the slow limit ($\Delta_{21}\to 0$), where φ becomes a quasistatic parameter that alters the system's stability landscape through the modulated drive amplitude,

$$|F_{\mathrm{eff}}|=F_1\sqrt{1+h^2+2h\cos(\theta_2-\theta_1-\varphi(T))}, \tag{14}$$

which oscillates between $F_{\mathrm{eff},-}\equiv F_1(1-h)$ and $F_{\mathrm{eff},+}\equiv F_1(1+h)$ as φ evolves. This modulation changes the rotating potential landscape, and hence the response of the system [see Fig. 2(b)].

Hereafter, we assume that the system is initialized in the low-amplitude stationary state of the single-tone problem (i.e., when $F_2=0$). The modulated amplitude of F_{eff} can trigger a jump if $|F_{\mathrm{eff}}|$ is large enough for the system to cross the lower branch bifurcation at Ω_1 [see Fig. 2(c)]. Thus, for the jumps to occur as φ is varied, $F_{\mathrm{eff},+}$ must satisfy or overshoot the discriminant condition for bifurcation [cf. Eq. (11)]. This leads to a critical value h_{lb} for the lower branch when $F_{\mathrm{eff},+}=F_{\mathrm{lb}}\equiv F_1(1+h_{\mathrm{lb}})$ exactly satisfies Eq. (11). For $h>h_{\mathrm{lb}}$, the system jumps when the low-amplitude attractor loses stability as φ is varied and moves to the high-amplitude attractor [see Fig. 2(c)]. Similarly, the high-amplitude branch bifurcates when $F_{\mathrm{eff},-}\leqslant F_{\mathrm{hb}}\equiv F_1(1-h_{\mathrm{hb}})$ and the system moves back to the low-amplitude attractor.

These *inter-attractor* jumps can be tracked by looking at the change in the stability of the attractors for varying φ and h in Fig. 2(d): For a circular trajectory at fixed $h>h_{\mathrm{lb}}$, as φ varies and F_{eff} changes, the system crosses the bifurcation point of the lower branch and consequently jumps to the available stationary branch and moves across stability regions where the low, high, or both branches are stable as in Fig. 2(e). This agrees with the recent experiment and analysis presented in Ref. [31]. However, when the beating between the tones

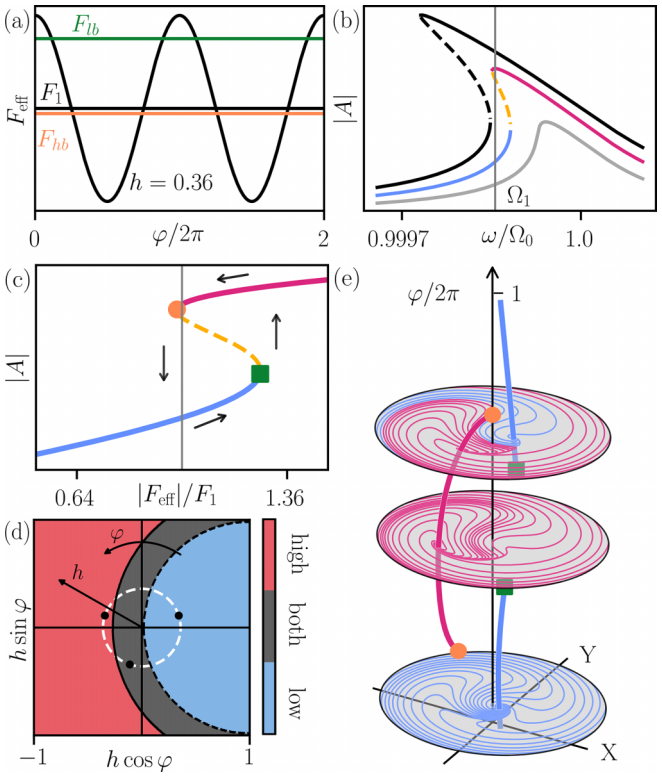


FIG. 2. The slow modulation picture. (a) The modulated effective drive amplitude $F_{\rm eff}$ over two cycles of the relative phase φ for $h = 0.36 > h_{\rm lb}$. The horizontal lines indicate the bifurcation thresholds $F_{\rm lb}$ (green) and $F_{\rm hb}$ (orange) [cf. Eq. (11)], and the primary tone's amplitude F_1 (black). (b) The stationary amplitude response as a function of drive frequency. The black (gray) curve shows the response at the maximum (minimum) $F_{\rm eff}^{\rm max(min)}$ for the modulation shown in panel (a). The colored lines show the response to a single drive, i.e., for $h = 0$ as in Fig. 1(c). The vertical gray line marks the frequency of the primary tone, Ω_1. (c) Bifurcation diagram against effective drive strength. As $|F_{\rm eff}|$ oscillates, the system follows the stable branches; arrows indicate the forced jumps between the low (blue) and high (pink) branches when thresholds are crossed. The orange circle (green square) marks $F_{\rm hb\,(lb)}$. The vertical gray line marks $|F_{\rm eff}| = F_1$. (d) Quasistatic phase diagram [cf. Eq. (12)] as a function of the relative drive strength h and phase $\varphi(T)$. The gray region marks bistability, separated by bifurcation thresholds (solid and dashed black arcs) to high- and low-branch-only regions. Dashed white circle: trajectory for $h = 0.36$. (e) Snapshot of vector flows at the three (black) points along the white trajectory in panel (d): monostable low (bottom), bistable (middle), and monostable high (top). The solid vertical arcs show the evolution of the blue (pink) low (high) branch as φ varies. Parameters: $\Omega_0 = 2\pi$, $\Gamma = 6.2 \times 10^{-4}$, and $F_1 = 4.81 \times 10^{-4}$.

becomes faster ($|\Delta_{21}| \gtrsim \Gamma$), the quasistatic picture breaks down, necessitating a more comprehensive analysis to capture the system's dynamics.

Building on Ref. [31], the decisive timescale for applying the quasistatic picture is the resonator ringdown, $\tau = 1/\Gamma$, which low-pass filters the beat-note modulation at $|\Delta_{21}|$. When $|\Delta_{21}| \ll \Gamma$ (beat period $\gg \tau$), the modulation is quasistatic: The vector flow evolves slowly and the state continuously follows the stationary branches until the branch bifurcates [Fig. 2(b)]. This enforces completed transitions between the low- and high-amplitude Duffing attractors once per cycle. Conversely, when $|\Delta_{21}| \lesssim \Gamma$ (beat period $\lesssim \tau$), the modulation is fast: Dissipation cannot relax the response to the changing attractor before it merges with the saddle, so the trajectory lags the changing flow and remains trapped near the initial basin, producing small loops without completed inter-attractor jumps despite an unchanged instantaneous vector flow with respect to the quasistatic case. Thus, naively, τ seems to set the boundary between slow transitions in Fig. 2(c) and fast, lagging dynamics. In the following, we show that this initial intuition from Ref. [31] does not depict the full picture.

Dynamical phase transitions

How do the trajectories change when the modulation is not infinitely slow? To answer this, we numerically solve Eq. (12), initializing the system in the low-amplitude stationary state of the single-tone case ($h = 0$) before introducing the secondary tone at $T = 0$. We look at the dynamics at a fixed, finite detuning Δ_{21} to understand the effect of the relative strength h on these transitions. The resulting amplitude dynamics $A(T)$ are contingent on h (see Fig. 3). For $h < h_{\rm lb}$, the initial lower-amplitude state is stable throughout the modulation and the system stays close to it [see Fig. 3(a)]. However, for $h > h_{\rm lb}$, we see two distinct types of behaviors. In Fig. 3(b), the amplitude of the system rises above the low-amplitude branch after it bifurcates, but never reaches the high-amplitude branch. In contrast, in Fig. 3(c), the system rises above the low-amplitude branch and reaches the high-amplitude branch during the modulation cycle.

To look at the complex dependence of the dynamics on Δ_{21} and h, we fix one parameter at small and large values and sweep across the other (see Fig. 4). The sharp jumps in $A(T)$ for $h > h_{\rm lb}$ in the slow-beating limit have the same period as the drive modulation [see Fig. 4(a)]. However, as the beating becomes faster ($\Delta_{21} \sim \Gamma$) the response accumulates a significant phase lag and changes smoothly [see Fig. 4(b)]. Furthermore, these dynamics are asymmetric with respect to Δ_{21}: Positively detuned secondary tones ($\Delta_{21} > 0$) trigger large amplitude variations over a wider range of detunings and lead to higher peak values than their negatively detuned ($\Delta_{21} < 0$) counterparts [see Figs. 4(c) and 4(d)]. The diverse nature of these amplitude dynamics across parameter space motivates using an effective quantity to distinguish the distinct dynamical regimes and track the transitions across these regimes.

We introduce the time-averaged amplitude over one drive modulation cycle, $\bar{A}$, defined as

$$\bar{A}(h, \Delta_{21}) = \frac{|\Delta_{21}|}{2\pi} \int_{T_0}^{T_0 + 2\pi/|\Delta_{21}|} A(T; h, \Delta_{21})\, \mathrm{d}T, \qquad (15)$$

with amplitude $A(T)$ obtained from the time evolution of Eq. (12). The cycle-averaged amplitude $\bar{A}$ serves as an order parameter for characterizing the system's long-term behavior. In Fig. 5, we present the phase diagram of $\bar{A}$ as a function of h and Δ_{21}, obtained from (a) experimental data measured on the setup (cf. Ref. [31] and Appendix C) and (b) numerical simulations. The $\bar{A}$ values of panel (a) are slightly lower than those of panel (b), suggesting that higher-order nonlinearities

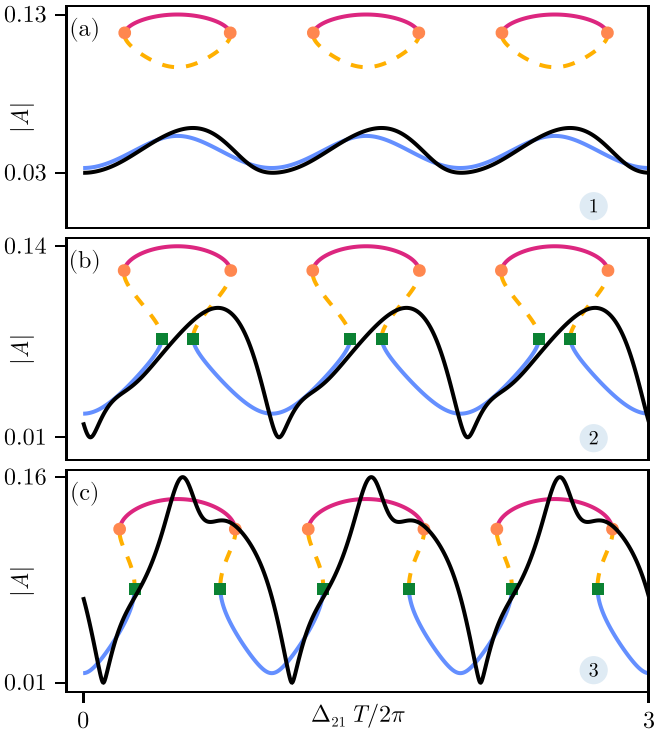


FIG. 3. The time-domain response $A(T)$ (black curve), simulated over three modulation cycles, attempting to follow the stationary states calculated from the quasistatic equation (12)—pink (blue) solid for high (low)-amplitude state and yellow dashed line for the saddle, with $\Delta_{21} = 0.42\Gamma$ for (a) $h = 0.1$, (b) $h = 0.33$, and (c) $h = 0.65$.

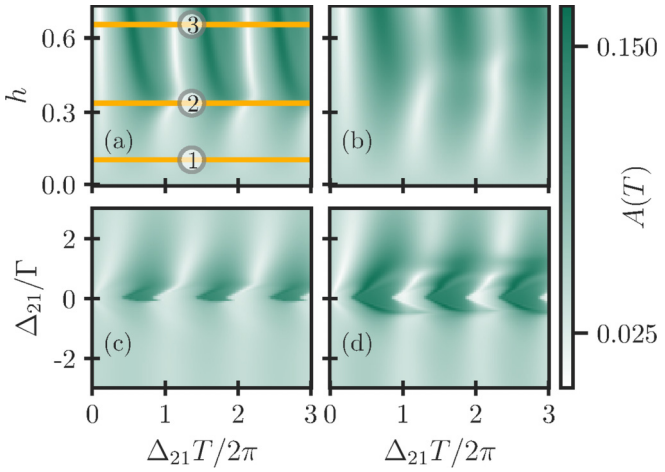


FIG. 4. Time-domain response amplitude $A(T)$ over three modulation cycles. (a) Slow modulation regime ($\Delta_{21} = 0.42\Gamma$): Numbered lines indicate cuts for $h = 0.1$ (stable low), $h = 0.33$ (deviation), and $h = 0.65$ (switching), corresponding to the trajectories in Fig. 3. (b) Same as panel (a) with fixed high detuning $\Delta_{21} = 0.91\Gamma$. The response exhibits significant phase lag and smooth changes compared with panel (a). (c) Fixed $h = 0.36$ with varying detuning: $\Delta_{21} > 0$ triggers larger amplitudes in response to the modulation than $\Delta_{21} < 0$. (d) Same as panel (c) with $h = 0.71$. Sharp dark green regions signal large amplitudes corresponding to jumps to the high-amplitude state.

may result in a saturated experimental response. We observe excellent agreement between panels (a) and (b) in terms of the overall shape of the high-$\bar{A}$ region, which validates our theoretical model [Eq. (12)].

In Fig. 5, we clearly distinguish between two dynamical regimes: dynamics confined to the low-amplitude attractor (low $\bar{A}$, light blue regions) and dynamics involving the high-amplitude attractor (high $\bar{A}$, dark regions), which encompass inter-attractor bursting oscillations and trajectories localized around the high-amplitude attractor. Interestingly, the transition boundary separating these two regimes is asymmetric: It is approximately linear in h for $\Delta_{21} < 0$ and appears parabolic for $\Delta_{21} > 0$. This representation clearly demarcates parameter regions associated with qualitatively different behaviors, particularly identifying the onset of inter-attractor jumps. Analytically determining this boundary in a general closed form, analogous to the single-tone approach [Eqs. (10) and (11)], is unfeasible due to the nonautonomous (i.e., explicitly time dependent) nature of the two-tone system [Eq. (12)]. The critical question then becomes: Can we approximate the boundary for these dynamical phase transitions, specifically the (h, Δ_{21}) conditions that precipitate such transitions?

VI. PHASE TRANSITION BOUNDARIES

In Sec. V, we observed that the secondary tone can lead to modulation and instabilities of the stationary response to the primary tone. In the slow modulation limit, we used Eq. (12) to argue that the response at frequency Ω_1 experiences a slow modulation due to the time-dependent effective drive amplitude in Eq. (13) and thus can exceed a threshold beyond which the initial single-tone branch destabilizes. However, this approach does not take into account the time it takes the system to respond to changes in the amplitude of the external drive, of order Γ^{-1}. In Fourier domain, this approach entails that we neglected the fact that the resonator has a different susceptibility to the secondary tone compared to the primary tone [cf. Fig. 1(b)]. As such, we cannot account for why the threshold in Fig. 5 increases with $|\Delta_{21}|$, nor why this increase occurs in an asymmetric fashion with respect to Δ_{21}.

To model the response of the system to the amplitude modulation of the external drive, we turn back to the power of the linear system at Ω_1, modulated due to the secondary tone [cf. Eq. (6) in Sec. III]. Indeed, the instability of the lower branch depends more on the amount of power actually received by the system, rather than the modulation amplitude of the external drive. Received power and drive amplitude are often closely associated, but under the conditions that we consider, they can diverge strongly: Consider, as an example, a high-amplitude modulation that is very fast, such that the system is unable to respond in time. The average power received by the system can then be very low, in spite of the high peak drive amplitude [cf. Fig. 4(d) for $\Delta_{21}/\Gamma = 2$].

In this section, we incorporate the information from linear response, i.e., the susceptibility function, on top of the stationary nonlinear motion of the Duffing resonator, to approximate the mechanism that allows for inter-attractor trajectories. We

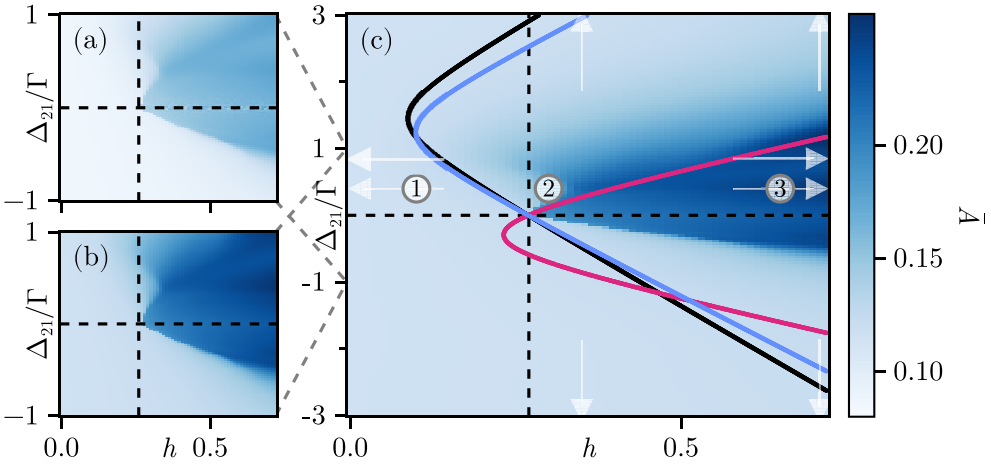


FIG. 5. The average amplitude in one modulation cycle, $\bar{A}$, as a function of relative strength h and frequency Δ_{21}. (a) Experimental data (adapted from Ref. [31]; cf. Appendix C). (b) Numerical simulation of Eq. (12). (c) Extended simulation range with analytical transition boundaries overlaid. The **black line** represents the instability threshold of the low-amplitude branch based on the bare resonance [cf. Eq. (17)]. The **pink line** represents the transition threshold incorporating the resonance frequency shift due to the high-amplitude state [cf. Eq. (19)]. The **blue line** uses the renormalized frequency of the low-amplitude state [cf. Eq. (20)]. Markers ①–③ correspond to the regimes illustrated in Fig. 3. The horizontal arrows correspond to the fixed Δ_{21} cuts and the vertical arrows correspond to fixed h cuts in Fig. 4.

first propose that the two-tone linear response power absorbed by the resonator [see Eq. (6)] serves as a good first approximation to the two-tone driven Duffing resonator. Second, we use this approximation to evaluate the filtered effective drive experienced at Ω_1. To this end, we use Eq. (6) to calculate the maximum and minimum linear response power, $A^2_{\Omega_{0,+}}$ and $A^2_{\Omega_{0,-}}$, respectively, achieved in a modulation cycle. Using the identity $\max_T[a_{\Omega_0}\cos(\Delta_{21}T)+b_{\Omega_0}\sin(\Delta_{21}T)] = \sqrt{a^2_{\Omega_0}+b^2_{\Omega_0}}$ at $T=\arctan(b_{\Omega_0}/a_{\Omega_0})/\Delta_{21}$, the expressions for the extrema read

$$A^2_{\Omega_{0,\pm}} = F_1^2(|\chi_1|^2+h^2|\chi_2|^2) \pm 2F_1^2 h|\chi_1|^2|\chi_2|^2\sqrt{a^2_{\Omega_0}+b^2_{\Omega_0}}, \tag{16}$$

where a_{Ω_0}, b_{Ω_0} are given by Eqs. (7) and (8). This maximum and minimum linear response power crucially depends on the strength and detuning of the secondary tone. Note that Eq. (16) describes the extremal received power at Ω_1 due to an off-resonant or detuned secondary tone. In contrast to Eq. (12), it ignores the Duffing nonlinearity but incorporates the effect of detuning.

Starting from Eq. (16), we use the linear susceptibility, χ_1 [cf. Eq. (2) for a single-tone drive], to formulate an in-phase effective (filtered) force $F_{\mathrm{eff}\,\Omega_{0,\pm}}$ that produces the same stationary response $A^2_{\Omega_{0,\pm}}$, at Ω_1,

$$F^2_{\mathrm{eff}\,\Omega_{0,\pm}} = A^2_{\Omega_{0,\pm}}/|\chi_1|^2. \tag{17}$$

This, in turn, enables us to find the effective drive amplitude required for a bifurcation at Ω_1, bringing us back to a similar threshold analysis as we explored in Sec. V.

The comparison between the effective drive strengths obtained in Eq. (17) and the critical drive amplitudes for bifurcation obtained in Eq. (11) provides us with the required force for jumping away from the lower branch toward the higher branch, i.e., $F_{\mathrm{eff}\,\Omega_{0,+}} \geqslant F_{\mathrm{lb}}$ [cf. Fig. 2(c)]. The threshold condition $F_{\mathrm{eff}\,\Omega_{0,+}} = F_{\mathrm{lb}}$ leads to the black transition threshold in Fig. 5(c). In Sec. V, the slow modulation allowed the system to reach the higher branch simply by leaving the lower one. With fast modulation, however, we must check that the system can still absorb sufficient power from the secondary tone during the jump. Indeed, as the system leaves the lower branch and approaches the higher branch, the oscillation amplitude grows, and the resonance frequency shifts with amplitude according to [36]

$$\Omega_{\mathrm{r}}(A) = \Omega_0\left(1+\frac{3\alpha}{8\Omega_0^2}A^2\right), \tag{18}$$

detuning the system from the secondary tone. This "dynamical" Duffing frequency shift (18) changes the filtered effective drive strength (17) and potentially prevents the transition to the higher branch. Therefore, completing the transition requires enough power to leave the lower branch and overcome resonance renormalization while keeping the absorbed power, and thus the filtered force in Eq. (17), above the F_{lb} threshold. We incorporate a conservative estimate of this effect using the amplitude of the higher branch, A_{high}, which is the target state of the transition once the lower branch destabilizes [cf. Fig. 2(c)], to calculate a renormalized filtered effective drive,

$$F^2_{\mathrm{eff}\,\Omega_{\mathrm{h},\pm}} = A^2_{\Omega_{\mathrm{h},\pm}}/|\chi_{\Omega_{\mathrm{h}}}(\Omega_1)|^2, \tag{19}$$

by combining Eqs. (16) and (18), defining the renormalized susceptibility $\chi_{\Omega_{\mathrm{h}}}(\Omega_1)$ and the renormalized absorbed power extrema $A^2_{\Omega_{\mathrm{h},\pm}}$, where $\Omega_{\mathrm{h}} \equiv \Omega_{\mathrm{r}}(A_{\mathrm{high}})$. The condition $F_{\mathrm{eff}\,\Omega_{\mathrm{h},+}} = F_{\mathrm{lb}}$ yields the transition boundary for the system to leave the lower branch and reach the higher branch during the modulation cycle [see pink curve in Fig. 5(c)].

In summary, two distinct thresholds govern the transition dynamics: The black line in Fig. 5(c) identifies the condition where the lower branch becomes unstable and the system is driven away from it, while the pink line identifies the regime where absorbed power from the secondary tone remains sufficient to cross the lower-branch instability

TABLE I. This table summarizes the different dynamical regions assuming a fixed primary tone in the bistability region, ①–⑧, differentiated by the starting branch [low (high) branch as lb (hb)] and the detuning and strength of the secondary tone. The properties of the secondary tone lead to different effective filtered drive strengths during modulation [see Eqs. (17) and (19)], which we call regimes. $F_{\rm hb}$ and $F_{\rm lb}$ are the bifurcation thresholds for the high and lower branches obtained in Eq. (11). $F_{{\rm eff}\,\Omega_{\rm h},\pm}$ is the maximum (minimum) renormalized filtered effective drive obtained in Eq. (19) that takes into account the dispersive shift [cf. Eq. (18)] due to the high-amplitude state $A_{\rm high}$. $F_{{\rm eff}\,\Omega_{\rm l},\pm}$ is the renormalized filtered effective drive that incorporates resonance renormalization due to the low-amplitude state $A_{\rm low}$. ①–③ refer to the cases presented in Figs. 3(a)–3(c) and marked on the phase diagram in Fig. 5(c). Cases ⑤–⑦ are presented in Figs. 9(a)–9(c) and are marked on the phase diagram in Fig. 10.

No.	Start branch	Regime	Outcome
①	lb	$F_{{\rm eff}\,\Omega_{\rm l},+} < F_{\rm lb}$	Stays lb
②	lb	$F_{{\rm eff}\,\Omega_{\rm l},+} < F_{\rm lb} < F_{{\rm eff}\,\Omega_{\rm h},+}$	lb + deviation
③	lb	$F_{\rm lb} < F_{{\rm eff}\,\Omega_{\rm l},+}, F_{{\rm eff}\,\Omega_{\rm h},+}$ and $F_{{\rm eff}\,\Omega_{\rm h},-} < F_{\rm hb}$	lb ↔ hb
④	lb	$F_{\rm lb} < F_{{\rm eff}\,\Omega_{\rm l},+}, F_{{\rm eff}\,\Omega_{\rm h},+}$ and $F_{{\rm eff}\,\Omega_{\rm h},-} > F_{\rm hb}$	Moves to hb and stays
⑤	hb	$F_{\rm hb} < F_{{\rm eff}\,\Omega_{\rm l},-}, F_{{\rm eff}\,\Omega_{\rm h},-}$	Stays hb
⑥	hb	$F_{{\rm eff}\,\Omega_{\rm h},-} < F_{\rm hb} < F_{{\rm eff}\,\Omega_{\rm l},-}$	hb + deviation
⑦	hb	$F_{{\rm eff}\,\Omega_{\rm l},-}, F_{{\rm eff}\,\Omega_{\rm h},-} < F_{\rm hb}$ and $F_{{\rm eff}\,\Omega_{\rm l},+}, F_{{\rm eff}\,\Omega_{\rm h},+} > F_{\rm lb}$	hb ↔ lb
⑧	hb	$F_{{\rm eff}\,\Omega_{\rm l},-}, F_{{\rm eff}\,\Omega_{\rm h},-} < F_{\rm hb}$ and $F_{{\rm eff}\,\Omega_{\rm l},+}, F_{{\rm eff}\,\Omega_{\rm h},+} < F_{\rm lb}$	Moves to lb and stays

and reach the higher branch, despite the amplitude-dependent frequency renormalization [cf. Eqs. (18) and (19)]. The interplay between these two thresholds explains the different dynamical regimes, which we illustrate with three representative trajectories: ① lies below both thresholds, where the trajectory remains confined to the lower branch as it remains stable throughout the modulation cycle [see Fig. 3(a)]; ② lies above the black but below the pink threshold, where the system departs from the lower branch but fails to reach the higher branch due to resonance frequency renormalization [see Fig. 3(b)]; and ③ lies above both thresholds, where the system possesses enough power to both destabilize the lower branch and complete the jump, successfully reaching the higher branch during its cycle [see Fig. 3(c)]. Importantly, the pink line provides a good approximation to the parabolic instability boundary observed in Fig. 5(c) for positive detuning ($\Delta_{21} > 0$), marking the success of our analytical approach.

Although our threshold estimates capture the main features of the two-tone dynamics, notable deviations arise for negative detuning ($\Delta_{21} < 0$), where the black transition threshold deviates significantly from the experimental/simulated transition. To improve this, we include resonance renormalization arising from the finite amplitude of the lower branch, $A_{\rm low}$, close to the system's initial state. We use Eq. (18) to define $\Omega_{\rm l} \equiv \Omega_{\rm r}(A_{\rm low})$ and correct Eq. (17) to get

$$F_{{\rm eff}\,\Omega_{\rm l},\pm} = A^2_{\Omega_{\rm l},\pm} \big/ |\chi_{\Omega_{\rm l}}(\Omega_{\rm l})|^2, \tag{20}$$

the renormalized filtered effective drive incorporating the shift due to $A_{\rm low}$. The resulting blue threshold line in Fig. 5(c) is closer to the observed transition for negative detunings ($\Delta_{21} < 0$). This points to the relevance of higher-order renormalization schemes, which could eventually reconcile the effective-drive model with the full nonlinear dynamics. Remaining discrepancies can be traced to (1) the coarse-grained nature of the time-averaged order parameter (15), which tends to smear transitions, and (2) the simplifying assumptions underlying our analytical treatment, which are intended to capture the qualitative threshold rather than its exact position. The latter motivates the study of the problem using a multifrequency ansatz.

Beyond the specific case studied here, other combinations of thresholds and trajectories are possible depending on the initial starting stationary state and the chosen primary tone detuning. For instance, starting from the higher branch, the system will leave the higher branch toward the lower branch if $F_{{\rm eff}\,\Omega_{\rm h},-} \leqslant F_{\rm hb}$ and will reach the lower branch if $F_{{\rm eff}\,\Omega_{0},-} \leqslant F_{\rm hb}$. These additional scenarios are systematically summarized in Table I, which maps the inequalities between $F_{{\rm eff}\,\Omega_{\rm h},+}$, $F_{{\rm eff}\,\Omega_{\rm h},-}$, $F_{\rm lb}$, and $F_{\rm hb}$ onto the corresponding dynamical outcomes. This overview highlights that the observed behavior is just one instance within a broader set of possible instability regimes, underscoring the richness of the system's driven dynamics (cf. Appendix B for additional examples). There, too, depending on the particular parameters used, the transition thresholds obtained from our model can deviate from the boundary observed in simulations. These deviations also trace back to the simplifying assumption of using a two-tone driven linear response to approximate the two-tone driven Duffing resonator's nonlinear response.

VII. EXTENSION OF THE ANSATZ

In Secs. V and VI, we analyzed how the secondary tone modifies the stationary response of the primary tone. The analysis stemmed from a quasistatic picture that focused on the secondary tone's influence on the response of the primary tone and ignored nonlinearity-induced interaction between the responses at the two tones. However, the complex beating patterns observed in Fig. 3 suggest that the interplay between the two drives generates dynamics that the single-tone ansatz [Eq. (3)] cannot capture. To clarify the spectral content of these dynamics, we compute the Fourier transform of the trajectories in Fig. 3. Tracking different Fourier components allows the definition of a "stationary state," even though the dynamics appear nonstationary in a single-frequency rotating frame. As shown in Fig. 6, the spectrum reveals a significant component at the detuning frequency $\omega = \Delta_{21}$, corresponding

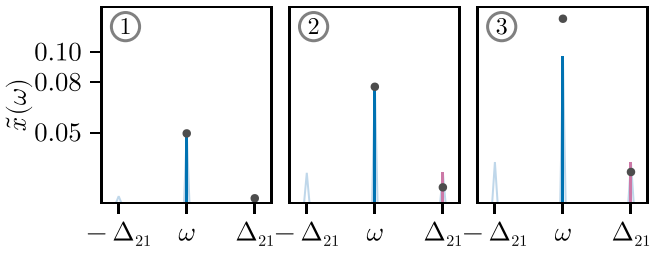


FIG. 6. Fourier spectra of the trajectories from Fig. 3. The peaks at $\omega = 0$ (blue) and $\omega = \Delta_{21}$ (pink) correspond to the response components at the primary tone Ω_1 and secondary tone Ω_2, respectively, in the Ω_1-rotating frame. Gray markers indicate the stationary state amplitudes A_1 and A_2 predicted by the multifrequency HBM ansatz [Eq. (22)]. The other parameters used are $\Omega_0 = 2\pi$, $\Gamma = 6.2 \times 10^{-4}$, $F_1 = 4.81 \times 10^{-4}$, and $\Delta_{10} = -9.02 \times 10^{-4}$.

to the Ω_2 response in the rotating frame. To capture this, we extend the single-tone ansatz [Eq. (3)] to a superposition of two rotating frames, treating both driving tones on an equal footing:

$$x(t) = \sum_{i=1,2} X_i(T)\cos(\Omega_i t) - Y_i(T)\sin(\Omega_i t), \tag{21}$$

where X_i, Y_i are the quadratures corresponding to the response at Ω_i.

We use the multifrequency ansatz (21) and apply the HBM, similar to Sec. IV. In the far-detuned regime ($\Delta_{21} \gg \Gamma$), the system's response time $\sim 2\pi/\Gamma$ is much longer than the beating period $2\pi/|\Delta_{21}|$. Thus, we can assume that the quadratures evolve on a timescale T much slower than the driving periods, $T_i = 2\pi/\Omega_i$. This yields four coupled first-order differential equations in X_i, Y_i:

$$\dot{X}_1 = -\frac{\Gamma}{2}X_1 + \left[\frac{\tilde{\Delta}_{01}^2}{2\Omega_1} + \frac{3\alpha}{4\Omega_1}\left(\frac{A_1^2}{2} + A_2^2\right)\right]Y_1 + \frac{F_1\sin\theta_1}{2\Omega_1}, \tag{22a}$$

$$\dot{Y}_1 = -\left[\frac{\tilde{\Delta}_{01}^2}{2\Omega_1} + \frac{3\alpha}{4\Omega_1}\left(\frac{A_1^2}{2} + A_2^2\right)\right]X_1 - \frac{\Gamma}{2}Y_1 + \frac{F_1\cos\theta_1}{2\Omega_1}, \tag{22b}$$

$$\dot{X}_2 = -\frac{\Gamma}{2}X_2 + \left[\frac{\tilde{\Delta}_{02}^2}{2\Omega_2} + \frac{3\alpha}{4\Omega_2}\left(\frac{A_2^2}{2} + A_1^2\right)\right]Y_2 + \frac{F_2\sin\theta_2}{2\Omega_2}, \tag{22c}$$

$$\dot{Y}_2 = -\left[\frac{\tilde{\Delta}_{02}^2}{2\Omega_2} + \frac{3\alpha}{4\Omega_2}\left(\frac{A_2^2}{2} + A_1^2\right)\right]X_2 - \frac{\Gamma}{2}Y_2 + \frac{F_2\cos\theta_2}{2\Omega_2}, \tag{22d}$$

where $A_i = \sqrt{X_i^2 + Y_i^2}$ is the response amplitude at frequency Ω_i, in analogy with Eq. (9). The nonlinearity introduces self-Kerr terms ($\propto A_i^2$), where the resonance frequency shifts based on the response at the tone itself, and cross-Kerr terms ($\propto A_j^2$), where the response at one tone shifts the effective resonance frequency of the other. These cross terms capture the nondegenerate four-wave mixing interactions that were averaged out in the single-tone slow-beating approximation. By balancing harmonics only at Ω_1 and Ω_2 to obtain Eq. (22), we neglect higher harmonics, e.g., $(3\Omega_i, 5\Omega_i)$ and mixed tones $(2\Omega_1 - \Omega_2, 2\Omega_2 - \Omega_1, \cdots)$.

Solving for the stationary states of Eq. (22) presents a significant challenge: The system comprises four coupled cubic polynomials with a theoretical upper limit of 81 solutions [55]. Standard local root-finding algorithms risk missing coexisting stable states in such a complex landscape. To overcome this, we use the HARMONICBALANCE.JL package [53], which relies on homotopy continuation [56]. This approach allows us to globally map the solution space, rigorously tracking the number and stability of all stationary states as we sweep the control parameters h and Δ_{21}.

We first study the effect of the relative drive strength h for a fixed detuning Δ_{21}. In Fig. 7, we plot the stationary response amplitudes A_1 and A_2 (at frequencies Ω_1 and Ω_2, respectively) as a function of h, assuming that the system is initialized in the low-amplitude attractor. For $h = 0$, the system reduces to the single-tone case and the amplitude at Ω_2 is 0. For positive detuning [$\Delta_{21} > 0$, see Fig. 7(a)], the response at Ω_2 increases steadily with h, while the response at Ω_1 remains initially confined to the low-amplitude state (blue branch in the A_1 panel). However, as the energy injected by the second tone increases with $h > 0.25$, the amplitude of this lower branch at Ω_1 rises rapidly until the branch destabilizes via a saddle-node bifurcation at $h = 0.65$. Beyond this critical threshold, the system transitions to the high-amplitude branch (pink branch in the A_1 panel) at Ω_1, which remains nearly constant, while the response at Ω_2 continues to increase with h.

The stationary states presented in Fig. 7(a) reveal the mechanism preventing the secondary tone from becoming the dominant spectral component, despite its proximity to the bare resonance. Initially, the system exhibits a linear response regime where A_2 grows proportionally to the drive strength h, corresponding to the stable dynamics of region ①. However, as the secondary amplitude becomes significant, the cross-Kerr interaction exerts a nonlinear frequency shift that pushes the tone's effective resonance frequency away from Ω_2 (toward lower frequencies for $\alpha < 0$). This interaction creates a scenario reminiscent of an avoided crossing between the responses at Ω_1 and Ω_2: Rather than A_2 capturing the input energy and increasing, beyond $h = 0.25$ it plateaus and the renormalization of the resonance frequency redistributes power to pump A_1, the response at Ω_1 (region ②). Consequently, the nonlinearity "protects" the dominance of the primary response A_1, as the growing secondary tone pushes the effective resonance further toward Ω_1. Ultimately, this cross-Kerr-induced pumping drives A_1 to a critical threshold where the low-amplitude branch destabilizes via a saddle-node bifurcation, forcing the transition to the high-amplitude attractor observed in region ③.

For negative detuning [$\Delta_{21} < 0$, see Fig. 7(b)], the stationary states display a distinct competition compared with the positive detuning case. The low-amplitude branch at A_1 and A_2 (solid blue line) remains stable over a wide range of h, with the primary response A_1 dominating. In contrast, the high-amplitude branch at A_1 and A_2 (solid pink line) exhibits a crossover where the secondary response A_2 grows rapidly, surpassing A_1 near $h \approx 0.5$, shortly before the branch destabi-

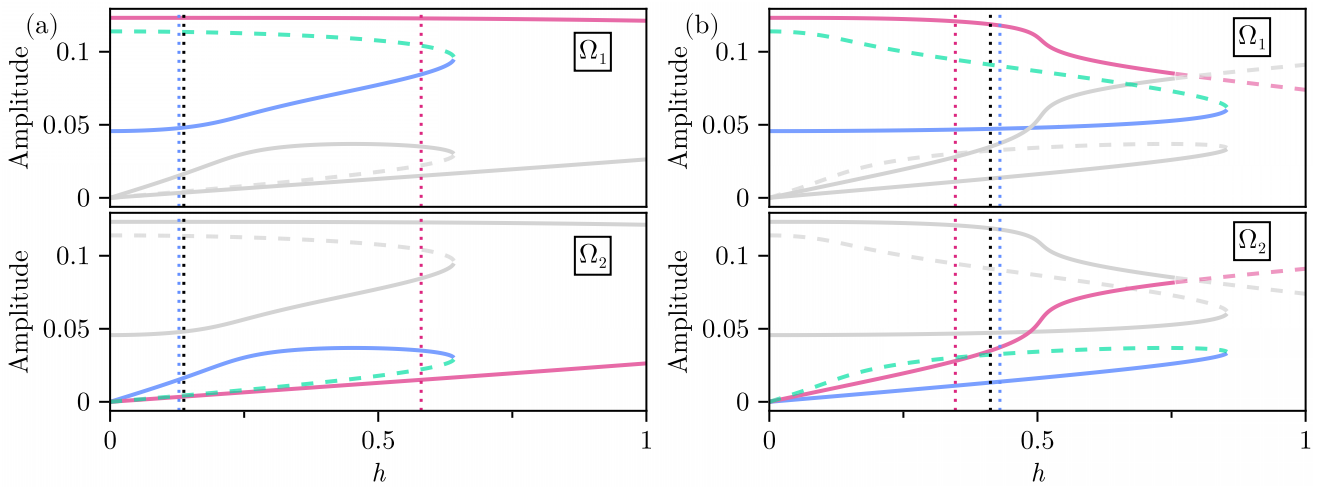


FIG. 7. Stationary states obtained from HBM using a multifrequency ansatz [cf. Eq. (22)] for fixed (a) $\Delta_{21} = 0.85\Gamma$ and (b) $\Delta_{21} = -0.85\Gamma$ as a function of h. The colored lines in the top (bottom) panel represent A_1 at Ω_1 (A_2 at Ω_2) and the gray lines represent A_2 (A_1). The colors identify the different branches: With respect to A_1, blue (pink) refers to the low (high)-amplitude response at the main drive tone; the corresponding amplitude A_2 is colored accordingly. The solid lines are stable branches and the dashed lines are saddles. The dotted vertical lines correspond to the (black, blue, and pink) transition boundaries shown in Fig. 5 for the respective Δ_{21}. Other parameters are $\Omega_0 = 2\pi$, $\Gamma = 6.2 \times 10^{-4}$, $F_1 = 4.81 \times 10^{-4}$, and $\Delta_{10} = -9.02 \times 10^{-4}$.

lizes. As $h \to 1$, a parameter window emerges where no stable states exist at the ansatz frequencies.

This behavior correlates directly with the transition thresholds discussed in Fig. 5. The low-amplitude branch at A_1 and A_2 persists because the secondary tone is far detuned from the bare resonance; it grows slowly and exerts negligible cross-Kerr influence on the primary mode. Conversely, for the high-amplitude state, the softening nonlinearity pulls the effective resonance frequency down, closer to the negatively detuned secondary tone. This reduces the effective detuning, enhancing the interaction through cross-Kerr terms and causing the branch to exhibit a large A_2. The crossover occurs in the vicinity of the blue/black transition threshold lines in Fig. 5; subsequently, the high-amplitude branch destabilizes, leaving the low-amplitude branch as the only available stable state. The absence of any stable states beyond $h = 0.775$ indicates that the slow-flow variables X_i, Y_i never settle to a fixed point but instead oscillate. This corresponds to a regime of limit cycle dynamics [57], manifesting physically as persistent, self-sustained amplitude modulations.

To map the global stability landscape, we repeat the process above as a function of h and Δ_{21}, counting the number of *stable* branches (see Fig. 8). The black horizontal lines ($\Delta_{21} \sim \Gamma$) represent the limit of spectral resolution of the tones; the two-tone HBM is robust for well-resolved tones (i.e., $|\Delta_{21}| > \Gamma$). For positive detunings ($\Delta_{21} > 0$), the numerically determined boundary where the system transitions from bistability (two stable branches, pink region) to monostability (one stable branch, green region) aligns remarkably well with the transition threshold derived from the high-amplitude renormalized filtered effective drive model (solid pink line). This confirms that, in the positively detuned regime ($\Delta_{21} > 0$), the transition is fundamentally governed by a strong enough drive overcoming the resonance frequency shift induced by the target state itself.

In contrast, the negative detuning region ($\Delta_{21} < 0$) reveals the breakdown of the stationary two-tone ansatz, consistent with the complex competition observed in Fig. 7(b). Here, the bifurcation boundaries diverge from the effective drive transition thresholds, indicating that the cross-Kerr interaction with the negatively detuned secondary tone induces parametric instabilities not captured by the simple resonance frequency shift model. We also observe that a distinct region emerges at high h where the number of stable stationary branches drops to zero (purple region). This absence of stable fixed points provides strong evidence for the formation of limit cycles, confirming that the dynamical phase transitions in the negatively detuned regime involve time-dependent nonstationary states rather than simple inter-attractor switching.

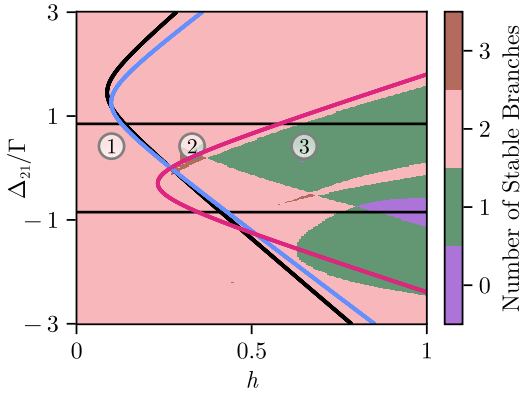


FIG. 8. The number of stable solutions plotted against varying Δ_{21} and h for fixed $\Omega_0 = 2\pi$, $\Gamma = 6.2 \times 10^{-4}$, $F_1 = 4.81 \times 10^{-4}$, and $\Delta_{10} = -9.02 \times 10^{-4}$. The black lines at $\Delta_{21} = \pm 0.85\Gamma$ reflect the cuts shown in Fig. 7. ①–③ represent the fixed parameters used for the trajectories in Figs. 3 and 6. The colored transition thresholds shown in Fig. 5 have been superposed for comparison. A region with zero stable fixed points (purple) emerges, indicative of limit cycle dynamics.

The multifrequency ansatz [cf. Eq. (21)] and the resulting equations of motion [cf. Eq. (22)] successfully capture the cross-Kerr interaction (nondegenerate four-wave mixing) between the system's responses to the two drives, providing physical insight beyond the linear and slow-beating approximations. The accuracy of this approach is confirmed in Fig. 6, where the HBM predictions at parameters ①–③ align well with the distinct Ω_1 and Ω_2 components extracted from the Fourier spectra of the time-domain trajectories. However, the method relies on the assumption of slowly varying envelopes, which is strictly valid only when the tones are spectrally resolved ($|\Delta_{21}| \gtrsim \Gamma$). As the system approaches the slow-modulation limit ($\Delta_{21} \to 0$), this timescale separation breaks down. This leads to deviations between the multiple sharp bifurcation thresholds predicted by the HBM and the transitions observed in the phase diagram (cf. Fig. 5), which are further broadened by the coarse graining inherent to the time-averaged order parameter $\bar{A}$. Finally, remaining discrepancies—particularly in the negative detuning regime—suggest that higher-order intermodulation products (e.g., $2\Omega_1 - \Omega_2$) neglected by the two-tone truncation may play a non-negligible role in the dynamics.

VIII. CONCLUSION AND OUTLOOK

In this work, we have developed a comprehensive framework to describe dynamical phase transitions in a Duffing resonator under bichromatic driving. By employing two complementary analytical approaches—an effective nonlinear response theory and an extended multifrequency ansatz—we have moved beyond phenomenological observation to uncover the distinct mechanisms governing the transitions in this system. Our analysis reveals that even a weak secondary tone can profoundly reshape the dynamics, not merely as a perturbation, but by fundamentally altering the stability landscape.

Our effective response theory provides a predictive tool for the slow-beating regime, where the secondary tone acts as a modulation that pushes the system past bifurcation points. Crucially, we identify that the onset of inter-attractor switching is not governed solely by the initial state, but by the resonance properties of the *target* state. Complementing this, our extended two-tone ansatz, valid in the resolved-sideband regime ($|\Delta_{21}| \gtrsim \Gamma$), reveals the microscopic mechanism behind these shifts. It reveals how cross-Kerr interactions (nondegenerate four-wave mixing) can either suppress switching via an avoided-crossing-like effect or induce instabilities leading to limit cycles, particularly in the negatively detuned ($\Delta_{21} < 0$) regime.

In contrast to earlier studies that surveyed specific parameters for sensing applications [29] or focused on cascades to chaos [30], we provided a rigorous mapping of the instability thresholds across a wide parameter space. This allowed us to explain the marked asymmetry between negative ($\Delta_{21} < 0$) and positive ($\Delta_{21} > 0$) detuning observed in experiments. Our results thereby offer a qualitative yet predictive framework to categorize dynamical phase transitions across nanomechanical [32], optical [37], and superconducting resonator [38,58] platforms.

Looking ahead, this framework lays the foundation for systematic extensions. The multifrequency approach can be expanded to include higher-order intermodulation products, analytically clarifying the route to chaos in multi-tone driven systems. Furthermore, our stability maps provide a basis for investigating how stochastic or quantum fluctuations mediate transitions near these newly identified thresholds [59]. Finally, in the context of strongly nonlinear Kerr resonators, these insights into controlled state-switching offer new protocols for quantum control and qubit operation [39,60], establishing multi-tone driving as a versatile resource for engineering dynamical phases.

ACKNOWLEDGMENTS

We acknowledge funding from the Deutsche Forschungsgemeinschaft (DFG) through Projects No. 449653034, No. 521530974, and No. 545605411, as well as via SFB 1432 (Project No. 425217212). We also acknowledge support from the Swiss National Science Foundation (SNSF) through the Sinergia Grant No. CRSII5_206008/1. J.d.P acknowledges funding from the Ramón y Cajal program (RYC2023-043827-I), funded by MICIU/AEI (10.13039/501100011033) and FSE+, and from the "María de Maeztu" Programme for Units of Excellence in R&D (CEX2023-001316-M), funded by the Spanish Ministry of Science, Innovation and Universities. J.d.P. also acknowledges support from the Proyectos de Generación de Conocimiento program, Grant No. PID2024 158923NA-I00, funded by MICIU/AEI (10.13039/501100011033) and FEDER, UE.

DATA AVAILABILITY

The data that supports the findings of this article are openly available [61].

APPENDIX A: DERIVATION OF THE LINEAR MODULATED POWER

In this Appendix, we provide a detailed derivation of the coupled equations of motion for the quadratures $X(t)$ and $Y(t)$ of a two-tone driven linear resonator, which are presented in Sec. III. Our starting point is the equation of motion for a linear damped harmonic oscillator, which is obtained by setting the nonlinearity $\alpha = 0$ in Eq. (1):

$$\ddot{x} + \Gamma\dot{x} + \Omega_0^2 x = \mathrm{Re}\left[\sum_{i=1,2} F_i e^{i(\Omega_i t + \theta_i)}\right]. \tag{A1}$$

We reformulate the problem in a frame corotating with the primary drive at frequency Ω_1. To this end, we employ the transformation for the resonator displacement $x(t)$ given in Eq. (3):

$$x(t) = X(t)\cos(\Omega_1 t) - Y(t)\sin(\Omega_1 t), \tag{A2}$$

with first and second time derivatives given by

$$\begin{aligned}\dot{x}(t) &= [\dot{X}(t) - \Omega_1 Y(t)]\cos(\Omega_1 t) \\ &\quad - [\dot{Y}(t) + \Omega_1 X(t)]\sin(\Omega_1 t), \qquad \text{(A3)}\\ \ddot{x}(t) &= [\ddot{X}(t) - 2\Omega_1\dot{Y}(t) - \Omega_1^2 X(t)]\cos(\Omega_1 t) \\ &\quad - [\ddot{Y}(t) + 2\Omega_1\dot{X}(t) - \Omega_1^2 Y(t)]\sin(\Omega_1 t). \qquad \text{(A4)}\end{aligned}$$

We decompose the second tone with respect to the first, using the detuning $\Delta_{21} = \Omega_2 - \Omega_1$, and set the drive phases to zero ($\theta_1 = \theta_2 = 0$), such that the total drive is $F(t) = F_1 \cos(\Omega_1 t) + F_2 \cos(\Omega_2 t)$. We express the second tone with reference to the rotating frame frequency Ω_1:

$$\begin{aligned} F(t) &= F_1 \cos(\Omega_1 t) + F_2 \cos(\Omega_1 t + \Delta_{21} t) \\ &= F_X(t) \cos(\Omega_1 t) + F_Y(t) \sin(\Omega_1 t), \end{aligned} \tag{A5}$$

with $F_X(t) = F_1(1 + h\cos(\Delta_{21} t))$ and $F_Y(t) = -hF_1 \sin(\Delta_{21} t)$ the time-dependent drive amplitudes into in-phase and quadrature components, for modulation amplitude $h = F_2/F_1$. We proceed by substituting the expressions for $x(t)$ and its derivatives [Eqs. (A2) and (A3)] and for the force [Eq. (A5)] into the equation of motion [Eq. (A1)]. We then apply the method of harmonic balancing by collecting all terms proportional to $\cos(\Omega_1 t)$ and $\sin(\Omega_1 t)$ and equating them, respectively, to $F_X(t)$ and $F_Y(t)$. We obtain

$$\begin{pmatrix} \partial_{tt} - \Omega_1^2 + \Omega_0^2 + \Gamma\partial_t & -2\Omega_1 \partial_t - \Gamma\Omega_1 \\ 2\Omega_1 \partial_t + \Gamma\Omega_1 & \partial_{tt} - \Omega_1^2 + \Omega_0^2 + \Gamma\partial_t \end{pmatrix} \vec{R} = \vec{F}_1(t), \tag{A6}$$

where $\partial_t \square \equiv \dot{\square}$ denotes the first time derivative, $\partial_{tt} \square \equiv \ddot{\square}$ the second time derivative, $\vec{R} = (X, Y)^T$, and $\vec{F}_1(t) = (F_X(t), F_Y(t))^T$. These equations fully describe the dynamics of the linear system in the rotating frame, accounting for the beating between the two drive tones.

The linear system in Eq. (A6) can be solved exactly by Fourier transforming the equations of motion, which converts them into coupled algebraic relations for the spectral amplitudes $\tilde{X}(\omega)$ and $\tilde{Y}(\omega)$. In this domain, each time derivative becomes $(i\omega)^n$, and the drives $F_X(t), F_Y(t)$ appear as Dirac delta peaks at $\omega = 0$ and $\omega = \pm\Delta_{21}$. Solving the algebraic system for $\tilde{X}(\omega)$ and $\tilde{Y}(\omega)$ and transforming back to time gives the quadratures $X(t)$ and $Y(t)$. The instantaneous power in the rotating frame is $A^2_{\Omega_0}(t, h) = X^2 + Y^2$, leading to the modulated response at Ω_1 shown in Eq. (6). To locate the extrema of the modulated power, we set $\partial_t A^2_{\Omega_0}(t, h) = 0$. Solving for the critical amplitudes gives the cycle's maximum and minimum power [cf. Eq. (16)]. This expression is central to the model developed in Sec. VI for determining the phase transition boundaries.

APPENDIX B: EXPLORATION OF MORE DYNAMICAL CASES

Our model's framework extends to other dynamical regimes. For instance, initializing the system on the high-amplitude branch captures the complementary transitions to Fig. 5(c), given by cases ⑤–⑧ in Table I and Fig. 9. The comparison of $F_{\text{eff}\,\Omega_-}$ with F_{hb} gives the threshold that correctly predicts the jumps down to the low branch in the corresponding phase diagram (see Fig. 10).

Conversely, when the system is initialized in the center of the bistability region, the model's quantitative agreement deviates (see Fig. 11). This is an expected outcome. Our model is based on a linear response approximation, which is most accurate on the quasilinear part of the branches [cf. Fig. 2(c)], i.e., far from their respective bifurcations. In the middle of the bistable region, the branches begin to deviate from the quasilinear behavior as they approach their respective bifurcations. Here, the system's response amplitude can no longer be approximated using the two-tone driven linear resonator's response [cf. Eq. (6)], leading to deviations between the predicted threshold and the simulations.

While asymptotic expansions can analyze such systems in the slow-modulation limit ($\Delta_{21} \ll \Gamma$) by leveraging timescale separation [27,28,62], our model's strength lies in providing a

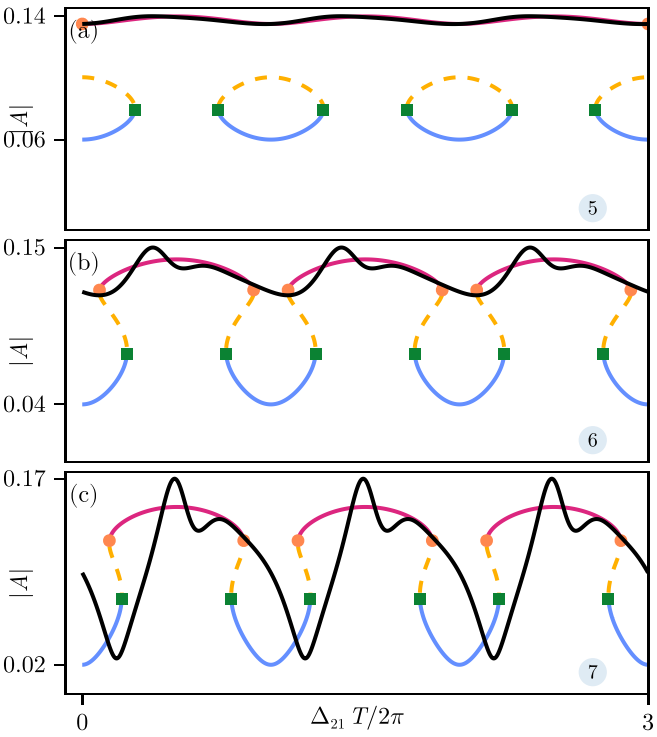


FIG. 9. The trajectories as in Fig. 3 for cases ⑤–⑦ in Table I for fixed detuning of the secondary tone, $\Delta_{21} = 0.45\Gamma$, and relative strength (a) $h = 0.07$, (b) $h = 0.275$, and (c) $h = 0.55$. The parameters used are $\Omega_0 = 2\pi$, $\Delta_{10} = -9.02 \times 10^{-4}$, $\Gamma = 6.2 \times 10^{-4}$, and $F_1 = 6.01 \times 10^{-4}$.

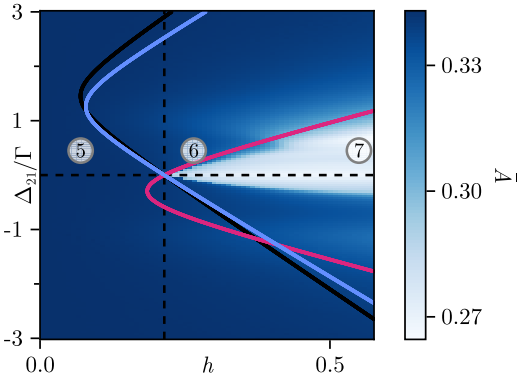


FIG. 10. The average amplitude phase diagram with threshold lines [cf. Fig. 5(c)], for an initial point starting from the higher branch, for $F_1 \sim F_{\text{lb}}$. The parameters used are $\Omega_0 = 2\pi$, $\Delta_{10} = -9.02 \times 10^{-4}$, $\Gamma = 6.2 \times 10^{-4}$, and $F_1 = 6.01 \times 10^{-4}$.

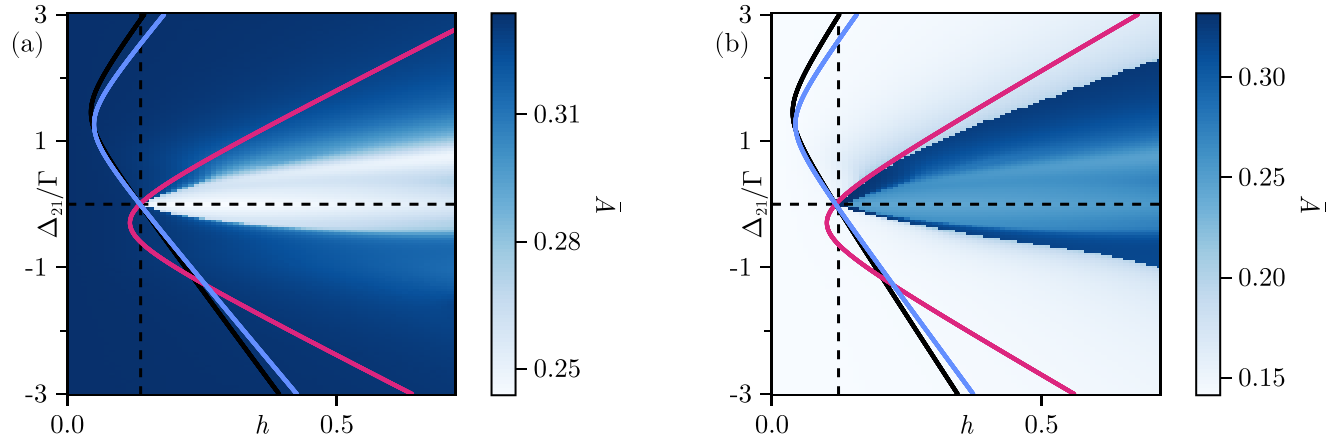


FIG. 11. The average amplitude phase diagram with threshold lines [cf. Fig. 5(c)] for an initial point in the middle of the bistability region. (a) The initial point starts from the higher branch. (b) The initial point starts from the lower branch. The parameters used are $\Omega_0 = 2\pi$, $\Delta_{10} = -9.02 \times 10^{-4}$, $\Gamma = 6.2 \times 10^{-4}$, and $F_1 = 5.46 \times 10^{-4}$.

qualitative and intuitive framework even when this separation is lost (i.e., as Δ_{21} approaches Γ). It successfully pinpoints the underlying mechanism—the competition between the drives due to the state-dependent resonance frequency—that governs the rich inter-attractor dynamics, offering a predictive tool where other analytical approaches are no longer applicable.

APPENDIX C: EXPERIMENTAL PLATFORM

Here, we provide details on the experimental setup and the measurement protocol used to generate Fig. 5(a). The experimental setup consists of a microelectromechanical system shaped as a double-ended tuning fork with branches 200 μm long and 6 μm thick. The device is capacitively coupled to gold electrodes fabricated next to it, which we can use to apply a driving voltage $U(t)$ and bias voltage U_b, and to read out the signal U_{out} containing the information about the resonator motion (see Fig. 12). The bias voltage is used to tune the resonance frequency and the Duffing parameter. The device is fabricated by Professor Kenny's group at Stanford [63] and is made out of highly doped single-crystal silicon with a p-type (boron) concentration of $1.5 \times 10^{20}\,\mathrm{cm}^{-3}$. The resonator is maintained at a pressure of 10^{-1} mbar through an epi-seal process [64].

The resonator vibration can be decomposed over a set of mechanical modes, which, in the limit of weak drive, can be individually described with the equation of motion of a simple damped harmonic oscillator:

$$\ddot{x} + \Omega_n^2 x + \Gamma_n \dot{x} = F_{\mathrm{dr}}(t), \tag{C1}$$

where Ω_n and Γ_n are the resonance frequency and the damping rate of the nth mode, respectively, and $F_{\mathrm{dr}}(t) = KU(t)$ is the applied drive in units of $\mathrm{V\,s^{-2}}$. K is a conversion factor expressed in units of $\mathrm{s^{-2}}$. When the strength of the external driving force increases, the resonator behavior starts to deviate from the standard damped harmonic oscillator. As we enter such large amplitude oscillation limit, to describe the system response to an external driving force we need to use the Duffing equation:

$$\ddot{x} + \Omega_n^2 x + \Gamma_n \dot{x} + \alpha_n x^3 = \mathrm{Re}[F_{\mathrm{dr}} e^{i(\Omega_{\mathrm{dr}} t + \theta)}], \tag{C2}$$

where α is the Duffing parameter in units of $\mathrm{V^{-2}\,s^{-2}}$.

In this work, we only focus on the lowest mechanical mode of the resonator. The mechanical parameters for this particular device have been characterized in a previous work [31] by measuring the amplitude (A) and phase (ϕ) response to an external drive in both the weak and strong drive limits. Using a lock-in amplifier, we apply an external driving force Ω_{dr} to the system, varying its value across the resonance Ω_0. With the same instrument, we simultaneously measure A and

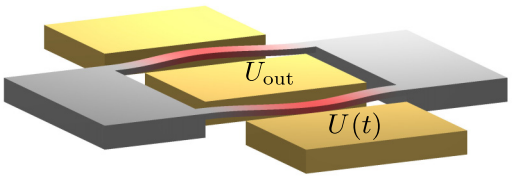


FIG. 12. Schematic representation of double-ended tuning fork device (adapted from Ref. [31]). The gray area represents the double-ended tuning fork with the vibrating part highlighted in red. The two outer gold pads represent the electrodes where we apply the driving voltage $U(t)$; the central one represents the one from which we readout the signal. The electrode for the bias voltage is not represented.

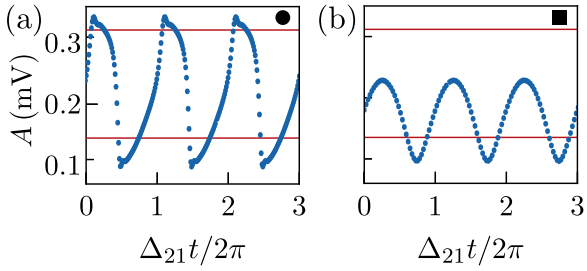


FIG. 13. Experimental phase diagram. Example of a measured $A(t)$ for (a) $\Delta_{21} < \Gamma$ and (b) $\Delta_{21} \approx \Gamma$ collected with the same F_1, Δ_{10}, and h. The upper (lower) red line represents the upper (lower) stable solution in the absence of the second drive (adapted from Ref. [31]).

ϕ in the frame rotating at $\Omega_{\rm dr}$. The measured mechanical parameters are $\Omega_0/2\pi = 1.11\,\text{MHz}$, $\Gamma/2\pi = 108\,\text{Hz}$, $\alpha = -1.89\,\text{V}^{-2}\,\text{s}^{-2}$, and $\text{K} \approx 1 \times 10^7\,\text{s}^{-2}$.

To generate the phase diagram in Fig. 5(a), we measure the resonator amplitude A as a function of time when driven with two different tones $F_1 e^{i(\Omega_1 t)}$ and $F_2 e^{i(\Omega_2 t)}$. We use the lock-in amplifier to apply the two driving tones and read out the amplitude in the frame rotating at Ω_1. After fixing $F_1/\text{K} = 140\,\text{mV}$ and $\Delta_{10}/2\pi \approx -158\,\text{Hz}$, we systematically probe the response of the resonator while varying $\Delta_{21} = \Omega_2 - \Omega_1$ and h. For each combination, we extract the average value $\bar{A}$ over an interval of 5 s making sure that for each combination the system is initialized in the lower stable solution of the Duffing curve before turning on the second drive. An example of measured $A(t)$ in the two limits of $\Delta_{21} < \Gamma$ and $\Delta_{21} \approx \Gamma$ is shown in Fig. 13.

[1] M. Dykman, *Fluctuating Nonlinear Oscillators: From Nanomechanics to Quantum Superconducting Circuits* (Oxford University Press, Oxford, 2012).

[2] R. Lifshitz and M. C. Cross, Nonlinear dynamics of nanomechanical and micromechanical resonators, in *Reviews of Nonlinear Dynamics and Complexity*, edited by H. G. Schuster (John Wiley & Sons, Ltd, Weinheim, 2008), Chap. 1, pp. 1–52.

[3] T. M. Lenton, H. Held, E. Kriegler, J. W. Hall, W. Lucht, S. Rahmstorf, and H. J. Schellnhuber, Tipping elements in the Earth's climate system, Proc. Natl. Acad. Sci. USA **105**, 1786 (2008).

[4] S. Strogatz, *Nonlinear Dynamics and Chaos: With Applications to Physics, Biology, Chemistry, and Engineering*, Studies in Nonlinearity (Westview Press, Cambridge, MA, 2007), repr. ed.

[5] L. Dai, D. Vorselen, K. S. Korolev, and J. Gore, Generic indicators for loss of resilience before a tipping point leading to population collapse, Science **336**, 1175 (2012).

[6] F. A. Buot, Mesoscopic physics and nanoelectronics: Nanoscience and nanotechnology, Phys. Rep. **234**, 73 (1993).

[7] E. Garmire, Nonlinear optics in daily life, Opt. Express **21**, 30532 (2013).

[8] M. Aspelmeyer, T. J. Kippenberg, and F. Marquardt, Cavity optomechanics, Rev. Mod. Phys. **86**, 1391 (2014).

[9] P. M. Harrington, E. J. Mueller, and K. W. Murch, Engineered dissipation for quantum information science, Nat. Rev. Phys. **4**, 660 (2022).

[10] B. van der Pol Jun, Lxxxviii. on "relaxation-oscillations", London, Edinburgh, Dublin Philos. Mag. J. Sci. **2**, 978 (1926).

[11] X. Liu, L. Pei, W. Wang, and S. Qi, Double Hopf bifurcation and stability of Koren–Feingold cloud–rain system with rain production delay, Eur. Phys. J.: Spec. Top. **231**, 2103 (2022).

[12] A. Asgari-Targhi and E. B. Klerman, Mathematical modeling of circadian rhythms, WIREs Syst. Biol. Med. **11**, e1439 (2019).

[13] D. J. DeShazer, J. García-Ojalvo, and R. Roy, Bursting dynamics of a fiber laser with an injected signal, Phys. Rev. E **67**, 036602 (2003).

[14] J. Moser, J. Güttinger, A. Eichler, M. J. Esplandiu, D. E. Liu, M. I. Dykman, and A. Bachtold, Ultrasensitive force detection with a nanotube mechanical resonator, Nat. Nanotechnol. **8**, 493 (2013).

[15] M. Poggio, Sensing from the bottom up, Nat. Nanotechnol. **8**, 482 (2013).

[16] A. Leuch, L. Papariello, O. Zilberberg, C. L. Degen, R. Chitra, and A. Eichler, Parametric symmetry breaking in a nonlinear resonator, Phys. Rev. Lett. **117**, 214101 (2016).

[17] J. Zhu, X. Liu, Q. Shi, T. He, Z. Sun, X. Guo, W. Liu, O. B. Sulaiman, B. Dong, and C. Lee, Development trends and perspectives of future sensors and MEMS/NEMS, Micromachines **11**, 7 (2019).

[18] L. Wei, X. Kuai, Y. Bao, J. Wei, L. Yang, P. Song, M. Zhang, F. Yang, and X. Wang, The recent progress of MEMS/NEMS resonators, Micromachines **12**, 724 (2021).

[19] G. Madiot, F. Correia, S. Barbay, and R. Braive, Bichromatic synchronized chaos in driven coupled electro-optomechanical nanoresonators, Phys. Rev. A **104**, 023525 (2021).

[20] B. Deng, M. Göb, B. A. Stickler, M. Masuhr, K. Singer, and D. Wang, Amplifying a zeptonewton force with a single-ion nonlinear oscillator, Phys. Rev. Lett. **131**, 153601 (2023).

[21] K. Sandholzer, A.-S. Walter, J. Minguzzi, Z. Zhu, K. Viebahn, and T. Esslinger, Floquet engineering of individual band gaps in an optical lattice using a two-tone drive, Phys. Rev. Res. **4**, 013056 (2022).

[22] Y. Wang, A.-S. Walter, G. Jotzu, and K. Viebahn, Topological Floquet engineering using two frequencies in two dimensions, Phys. Rev. A **107**, 043309 (2023).

[23] Y. Chen, Z. Zhu, and K. Viebahn, Mitigating higher-band heating in Floquet-Hubbard lattices via two-tone driving, Phys. Rev. A **112**, L021301 (2025).

[24] X. Qiu, S. Kumar, F. A. Cárdenas-López, G. Alvarado Barrios, E. Solano, and F. Albarrán-Arriagada, Microwave quantum memcapacitor effect, Commun. Mater. **5**, 70 (2024).

[25] Z.-X. Liu, J. Peng, and H. Xiong, Generation of magnonic frequency combs via a two-tone microwave drive, Phys. Rev. A **107**, 053708 (2023).

[26] M. Yarmohammadi, Dynamical phase transition in a strongly hybridized phonon-triplon chain, Phys. Rev. B **112**, 144432 (2025).

[27] M. Desroches, J. Guckenheimer, B. Krauskopf, C. Kuehn, H. M. Osinga, and M. Wechselberger, Mixed-mode oscillations with multiple time scales, SIAM Rev. **54**, 211 (2012).

[28] M. Desroches, J.-P. Francoise, and M. Krupa, Parabolic bursting, spike-adding, dips and slices in a minimal model, Math. Model. Nat. Phenom. **14**, 406 (2019).

[29] S. Houri, R. Ohta, M. Asano, Y. M. Blanter, and H. Yamaguchi, Pulse-width modulated oscillations in a nonlinear resonator under two-tone driving as a means for MEMS sensor readout, Jpn. J. Appl. Phys. **58**, SBBI05 (2019).

[30] S. Houri, M. Asano, H. Yamaguchi, N. Yoshimura, Y. Koike, and L. Minati, Generic rotating-frame-based approach to chaos generation in nonlinear micro- and nanoelectromechanical system resonators, Phys. Rev. Lett. **125**, 174301 (2020).

[31] L. Catalini, J. del Pino, S. S. Kumar, V. Dumont, G. Margiani, O. Zilberberg, and A. Eichler, Slow and fast topological

dynamical phase transitions in a Duffing resonator driven by two detuned tones, Phys. Rev. Res. **7**, 033058 (2025).

[32] L. Michaeli, R. Gao, M. D. Kelzenberg, C. U. Hail, J. E. Sader, and H. A. Atwater, Optically actuated transitions in multimodal, bistable micromechanical oscillators, arXiv:2507.22605.

[33] M. O. Scully and M. S. Zubairy, *Quantum Optics* (Cambridge University Press, Cambridge, 1997).

[34] N. M. Krylov and N. N. Bogoljubov, *Introduction to Non-Linear Mechanics: AM-11*, Annals of Mathematics Studies No. 11 (Princeton University Press, Princeton, NJ, 2016).

[35] A. H. Nayfeh and D. T. Mook, *Nonlinear Oscillations* (Wiley, New York, 1995).

[36] A. Eichler and O. Zilberberg, *Classical and Quantum Parametric Phenomena* (Oxford University Press, Oxford, 2023).

[37] N. Carlon Zambon, S. R. K. Rodriguez, A. Lemaître, A. Harouri, L. Le Gratiet, I. Sagnes, P. St-Jean, S. Ravets, A. Amo, and J. Bloch, Parametric instability in coupled nonlinear microcavities, Phys. Rev. A **102**, 023526 (2020).

[38] A. Blais, A. L. Grimsmo, S. M. Girvin, and A. Wallraff, Circuit quantum electrodynamics, Rev. Mod. Phys. **93**, 025005 (2021).

[39] V. John, F. Borsoi, Z. György, C.-A. Wang, G. Széchenyi, F. van Riggelen-Doelman, W. I. L. Lawrie, N. W. Hendrickx, A. Sammak, G. Scappucci, A. Pályi, and M. Veldhorst, Bichromatic Rabi control of semiconductor qubits, Phys. Rev. Lett. **132**, 067001 (2024).

[40] M. Scheffer, J. Bascompte, W. A. Brock, V. Brovkin, S. R. Carpenter, V. Dakos, H. Held, E. H. van Nes, M. Rietkerk, and G. Sugihara, Early-warning signals for critical transitions, Nature (London) **461**, 53 (2009).

[41] C. Kuehn, A mathematical framework for critical transitions: Bifurcations, fast–slow systems and stochastic dynamics, Physica D **240**, 1020 (2011).

[42] C. Kuehn, K. Lux, and A. Neamţu, Warning signs for non-Markovian bifurcations: Colour blindness and scaling laws, Proc. R. Soc. A **478**, 20210740 (2022).

[43] Note that the Fourier transform assumes the signal is defined for all time, effectively requiring an infinitely long observation.

[44] G. B. Arfken, H.-J. Weber, and F. E. Harris, *Mathematical Methods for Physicists: A Comprehensive Guide*, 7th ed. (Academic Press, Waltham, MA, 2013).

[45] S. Mukamel, *Principles of Nonlinear Optical Spectroscopy*, Oxford series in optical and imaging sciences (Oxford University Press, Oxford, 1999).

[46] M. Soriente, T. L. Heugel, K. Omiya, R. Chitra, and O. Zilberberg, Distinctive class of dissipation-induced phase transitions and their universal characteristics, Phys. Rev. Res. **3**, 023100 (2021).

[47] T. L. Heugel, A. Eichler, R. Chitra, and O. Zilberberg, The role of fluctuations in quantum and classical time crystals, SciPost Phys. Core **6**, 053 (2023).

[48] V. Dumont, M. Bestler, L. Catalini, G. Margiani, O. Zilberberg, and A. Eichler, Energy landscape and flow dynamics measurements of driven-dissipative systems, Phys. Rev. Res. **6**, 043012 (2024).

[49] G. Villa, J. del Pino, V. Dumont, G. Rastelli, M. Michałek, A. Eichler, and O. Zilberberg, Topological classification of driven-dissipative nonlinear systems, Sci. Adv. **11**, eadt9311 (2025).

[50] A. H. Nayfeh, *Perturbation Methods*, 1st ed. (Wiley, Weinheim, 2000).

[51] R. Rand, *Lecture Notes on Nonlinear Vibrations* (The Internet-First University Press, Ithaca, N.Y., 2012).

[52] M. Krack and J. Gross, *Harmonic Balance for Nonlinear Vibration Problems, Mathematical Engineering* (Springer International Publishing, Cham, 2019).

[53] J. Košata, J. Del Pino, T. L. Heugel, and O. Zilberberg, HarmonicBalance.jl: A Julia suite for nonlinear dynamics using harmonic balance, SciPost Phys. Codebases 6 (2022).

[54] L. Papariello, O. Zilberberg, A. Eichler, and R. Chitra, Ultrasensitive hysteretic force sensing with parametric nonlinear oscillators, Phys. Rev. E **94**, 022201 (2016).

[55] E. Bézout, Théorie générale des équations algébriques, De l'imprimerie de Ph.-D. Pierres, rue S. Jacques, A Paris, 1779.

[56] P. Breiding and S. Timme, HomotopyContinuation.jl: A package for homotopy continuation in Julia, in *Mathematical Software—ICMS 2018*, edited by J. H. Davenport, M. Davenport, G. Labahn, and J. Urban (Springer International Publishing, Cham, 2018), pp. 458–465.

[57] J. del Pino, J. Košata, and O. Zilberberg, Limit cycles as stationary states of an extended harmonic balance ansatz, Phys. Rev. Res. **6**, 033180 (2024).

[58] F. Fani Sani, I. C. Rodrigues, D. Bothner, and G. A. Steele, Level attraction and idler resonance in a strongly driven Josephson cavity, Phys. Rev. Res. **3**, 043111 (2021).

[59] M. Marthaler and M. I. Dykman, Switching via quantum activation: A parametrically modulated oscillator, Phys. Rev. A **73**, 042108 (2006).

[60] J. A. Valery, S. Chowdhury, G. Jones, and N. Didier, Dynamical sweet spot engineering via two-tone flux modulation of superconducting qubits, PRX Quantum **3**, 020337 (2022).

[61] https://github.com/soumyasrtk/dpt_twotonedrive_duffing.

[62] J. Zhu, R. Kuske, and T. Erneux, Tipping points near a delayed saddle node bifurcation with periodic forcing, SIAM J. Appl. Dyn. Syst. **14**, 2030 (2015).

[63] M. Agarwal, S. A. Chandorkar, H. Mehta, R. N. Candler, B. Kim, M. A. Hopcroft, R. Melamud, C. M. Jha, G. Bahl, G. Yama, T. W. Kenny, and B. Murmann, A study of electrostatic force nonlinearities in resonant microstructures, Appl. Phys. Lett. **92**, 104106 (2008).

[64] Y. Yang, E. J. NG, Y. Chen, I. B. Flader, and T. W. Kenny, A unified epi-seal process for fabrication of high-stability microelectromechanical devices, J. Microelectromech. Syst. **25**, 489 (2016).